

Stable discontinuous staggered grid in the finite-difference modelling of seismic motion

Jozef Kristek,^{1,2} Peter Moczo^{1,2} and Martin Galis^{1,2}

¹Faculty of Mathematics, Physics and Informatics, Comenius University Bratislava, Mlynska dolina F1, 842 48 Bratislava, Slovak Republic.

E-mail: moczo@fmph.uniba.sk

²Geophysical Institute, Slovak Academy of Sciences, Dubravska cesta 9, 845 28 Bratislava, Slovak Republic

Accepted 2010 August 13. Received 2010 August 2; in original form 2010 April 6

SUMMARY

We present an algorithm of the spatial discontinuous grid for the 3-D fourth-order velocity–stress staggered-grid finite-difference modelling of seismic wave propagation and earthquake motion. The ratio between the grid spacing of the coarser and finer grids can be an arbitrary odd number. The algorithm allows for large numbers of time levels without inaccuracy and eventual instability due to numerical noise inevitably generated at the contact of two grids with different spatial grid spacings. The key feature of the algorithm is the application of the Lanczos downsampling filter.

The algorithm of the discontinuous grid is directly applicable also to the displacement–stress staggered-grid finite-difference scheme.

Key words: Computational seismology; Theoretical seismology; Wave propagation.

1 INTRODUCTION

If the minimum wave speed in an upper part of a computational model is smaller than that in a lower part of the model, it may be reasonable to use a finer grid (with the grid spacing h) covering the upper part of the model and a coarser grid (with the grid spacing $H > h$) covering the lower part of the model. A total number of gridpoints in such a discontinuous spatial grid can be significantly smaller than that in a uniform grid. This simple idea led modellers that use grid methods, mainly the finite-difference (FD) method, to implement discontinuous grids in their numerical modelling.

Jastram & Behle (1992) introduced a discontinuous grid in their 2-D acoustic, conventional-grid FD time-domain (FDTD) modelling. Their grid enabled to choose an arbitrary integer ratio of the coarser-grid spacing H to finer-grid spacing h , that is $H/h = 2, 3, \dots$. They used trigonometric interpolation in the horizontal direction to calculate pressure at the missing positions in the coarser grid near the contact with the finer grid. Jastram & Tessmer (1994) generalized the concept in their 2-D P-SV elastic displacement–stress staggered-grid FDTD modelling. The grid enabled $H/h = 3, 5, 7, \dots$. They applied trigonometric interpolation to displacement and stress-tensor components. Wang & Schuster (1996) extended the approach by Jastram & Tessmer (1994) to 3-D and axisymmetric fourth-order FDTD simulations.

Moczo *et al.* (1996) used an adjusted FD approximation at the contact of the $H/h = 2$ discontinuous grid in their second-order 2-D SH elastic, conventional-grid FDTD. The use of the adjusted FD approximation enabled to avoid an interpolation of the displacements at the missing grid positions.

Kristek *et al.* (1999) applied a $H/h = 3$ discontinuous grid in their 3-D fourth-order, viscoelastic, displacement–stress staggered-

grid FDTD modelling. They applied linear interpolation in a horizontal grid plane. Aoi & Fujiwara (1999) applied a $H/h = 3$ discontinuous grid in their 3-D second-order viscoelastic, velocity–stress staggered-grid FDTD. They used linear interpolation in a horizontal grid plane. Wang *et al.* (2001) applied a $H/h = 2, 3, \dots$ discontinuous grid in their 3-D fourth-order, viscoelastic, velocity–stress staggered-grid FDTD. They used a 3-D interpolation in the wavenumber domain. Moczo *et al.* (2007) applied a $H/h = 3, 5, 7, \dots$ discontinuous grid in their 3-D fourth-order, viscoelastic, velocity–stress staggered-grid FDTD.

Wang & Takenaka (2001) applied a $H/h = 2$ discontinuous grid in the 2-D P-SV elastic, conventional-grid Fourier pseudospectral modelling with interpolation in the wavenumber domain. Hayashi *et al.* (2001) applied a $H/h = 3$ discontinuous grid in their 2-D P-SV fourth-order, viscoelastic, velocity–stress staggered-grid FDTD.

Unlike other modellers, Robertsson & Holliger (1997) incorporated a $H/h = 2$ discontinuous grid to accommodate a free-surface topography in their 3-D velocity–stress staggered-grid FDTD modelling. Because in their method the non-planar free surface requires finer spatial discretization compared to the underlying interior, they covered it with a finer grid. They applied linear interpolation in the vertical direction and sinc interpolation in the horizontal direction. Also atypically, Moczo *et al.* (1997) used finite-elements as the contact zone between h and $2h$ FD grids in their 2-D P-SV viscoelastic modelling.

Kang & Baag (2004a) presented a computationally efficient combination of the spatial discontinuous velocity–stress staggered grid with a locally varying time step for 2-D and 3-D higher-order FDTD modelling. Kang & Baag (2004b) further increased the computational efficiency by elaborating a discontinuous grid with a laterally localized finer grid with a locally varying time step.

Chaljub *et al.* (2003) implemented a discontinuous spherical grid in their spectral-element modelling of the elastic wave propagation in a solid-fluid sphere using the so-called mortar method. At the contact of the finer and coarser grids two neighbouring elements do not share an entire edge or entire face.

We can also mention a work of Kopriva (1989) about non-matching (i.e. spatially different) pseudospectral grids. His approach is close to the methodology of the non-matching mortar spectral-element grids. Finally, it is worth noticing an interesting conservative space–time mesh refinement applied to the FDTD solution of Maxwell's equations by Collino *et al.* (2006).

It is obvious that a number of algorithms to include discontinuous spatial grid have been developed. The algorithms mainly differ in the allowed grid ratio H/h and the way they interpolate values in the missing grid positions in the coarser grid.

In general, one could guess, the larger is the grid ratio H/h , the larger is the possibility of inaccuracy and, mainly, instability with an increasing number of time steps due to a numerical noise that is generated at the contact of the finer and coarser grids. At the same time, it is obvious that the noise generation and possible instability cannot simply correlate with the grid ratio—they may strongly depend on the material and wavefield heterogeneity. The possibility of instability is only rarely explicitly addressed in the publications on the FD modelling. Among the rare exceptions, De Lilla (1997) points out that as the grid ratio increases, the numerical inaccuracy due to the change of the grid spacing may increase. Hayashi *et al.* (2001) explicitly say that $H/h = 3$ is better for stability and accuracy compared to higher ratios. To reduce instability, they apply certain averaging or weighting to the replacement of the coarse-grid components within the fine-grid field. Their procedure enables them to have computation stable during several thousands time steps.

In an implementation of a discontinuous spatial grid there are two basic problems to be solved. The very obvious problem is that of the missing gridpoints. This is the reason for interpolation. The other and apparently not so obvious, problem is how to update particle velocity and stress at those gridpoints of the coarser grid, which coincide with gridpoints of the finer grid.

In this paper, we present an algorithm of a stable discontinuous staggered-grid. The grid ratio H/h can be an arbitrary odd number. We demonstrate that our algorithm is capable to reduce inaccuracy due to artificial numerical noise and prevent instability possibly caused by the numerical noise in case of large number of time steps.

2 PRELIMINARY CONSIDERATIONS ON THE DISCONTINUOUS STAGGERED GRID

Fig. 1 shows a spatial-grid cell in a 3-D velocity–stress staggered grid. Each of the three particle-velocity components and three shear stress-tensor components has its own spatial-grid position. The three normal stress-tensor components share another grid position. The structure of the staggered grid implies that the most natural grid ratio H/h of a discontinuous grid is an odd number. The simplest case is that of $H/h = 3$: Consider, for example, a grid position of the xz -stress-tensor component. The calculation of the xz -component requires the x -derivative of the z -particle-velocity component. In the given grid the nearest z -particle-velocity components are located at distances $0.5h$ to the left and to the right from the position of the xz -stress-tensor component. If we omit these two nearest positions, the next available positions of the z -particle-velocity components

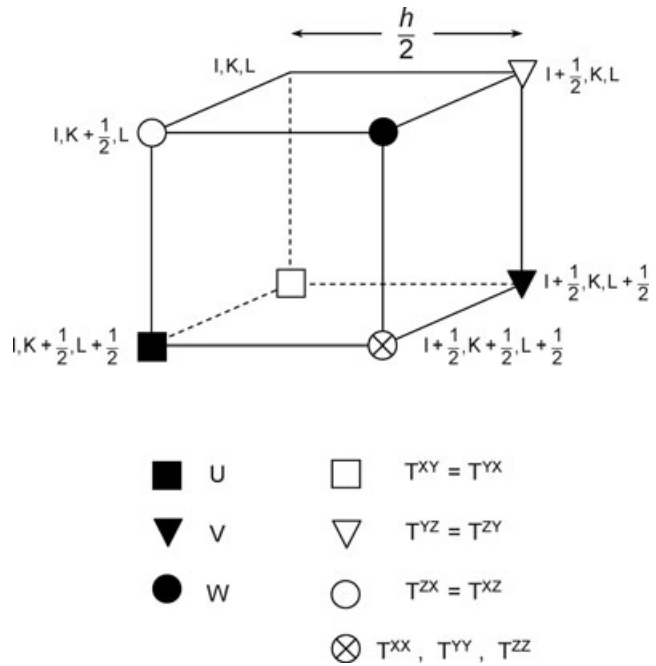


Figure 1. Spatial-grid cell in a 3-D velocity–stress staggered grid.

are at distances $1.5h$ to the left and to the right from the considered position of the xz -stress-tensor component. This gives a grid spacing of $H = 3h$ between two positions of the z -particle-velocity components in the coarser grid.

Consider a hypothetical situation with a horizontal material interface between an upper medium with smaller shear-wave speed and a lower medium with larger shear-wave speed. One might speculate about a desirable (most economical) discontinuous grid with a finer grid ending and a coarser grid starting just at the material interface. Such a grid would not be a good solution: the fourth-order interior FD formula would require interpolated values at distances of $0.5h$ and $1.5h$ from the interface in the medium with a larger wave speed. Such an interpolation would lead to considerable inaccuracy. An alternative would be the use of the fourth-order one-sided approximations (spatial extent of $3.5h$ in the vertical direction) in the upper medium. A one-sided approximation is, in fact, an equivalent of extrapolation. Therefore, it should not be applied if it is possible to apply a centred approximation. Consequently, it is much better to place the boundary of the finer grid in the medium with the larger wave speed. The finer and coarser grids then overlap in the medium with the larger wave speed.

Even if there is no material interface and, instead, the wave speed smoothly increases, it is obvious that the finer and coarser grid should reasonably overlap.

The definition of the boundary of the finer grid and the overlapping zone depends on the solutions to two basic problems. The very obvious problem, addressed in all published articles, is the problem of the missing grid positions of the particle-velocity and stress-tensor components needed for updating these quantities close and at the boundary of the finer grid. The other, and apparently not so obvious, problem is how to update particle-velocity and stress-tensor components at gridpoints of the coarser grid close and at the boundary of the coarser grid, that is, at those gridpoints of the coarser grid, which coincide with the gridpoints of the finer grid.

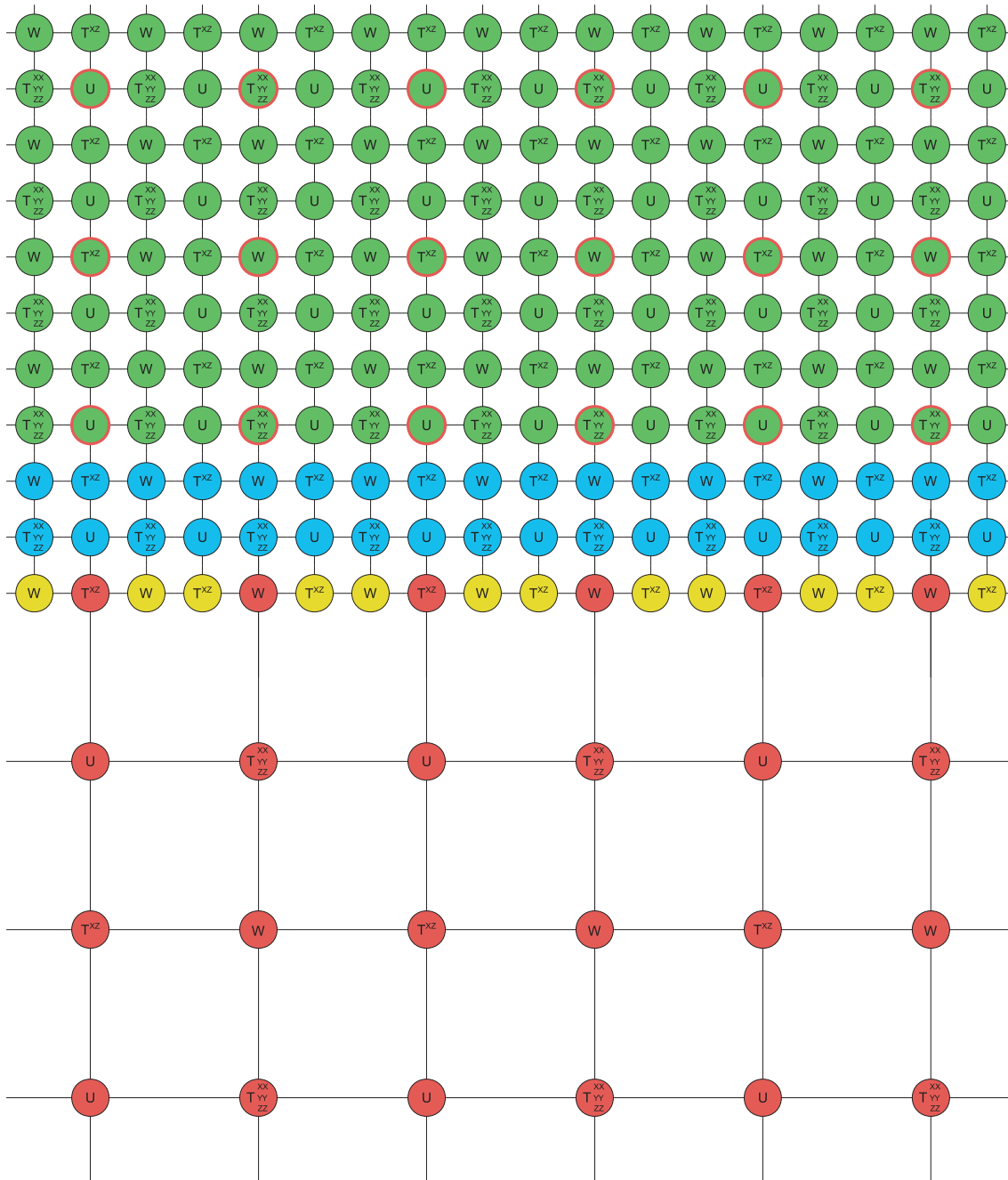


Figure 2. A vertical xz -grid plane in the simplest case of a spatial discontinuous velocity–stress staggered grid. The boundaries of the grid are not shown.

3 THE VELOCITY–STRESS DISCONTINUOUS STAGGERED GRID

Fig. 2 shows a vertical grid plane of a spatial velocity–stress discontinuous staggered grid. Only the grid plane with positions of the normal stress-tensor components in both the finer and coarser grids is shown. The vertical grid plane with the xy -stress-tensor components in both grids is analogous. Obviously, there are also vertical grid planes with the finer grid only. Fig. 2 shows the simplest possible configuration of the discontinuous grid, that is, the case with $H/h = 3$. The grid ratio, however, can be an arbitrary odd number: $H/h = 3, 5, 7, \dots$. This is an important aspect.

In Fig. 2 the interior grid positions of the finer grid are in green colour. The particle-velocity and stress-tensor components at these positions are updated using the interior fourth-order FD scheme in the finer grid. The boundary of the finer grid is made of one grid row of cells with the blue grid positions. The yellow colour indicates grid positions at which values have to be interpolated; these values are necessary for updating values at the blue grid positions. The red colour indicates interior-grid positions of the coarser grid. The particle-velocity and stress-tensor components at these positions are updated using the interior fourth-order FD scheme in the coarser grid. The red-circumscribed green positions define the boundary of the coarser grid.

To define the algorithm of the described discontinuous grid, we have to specify how to update field values at blue, yellow and red-circumscribed green grid positions.

3.1 Boundary of the finer grid in the overlapping zone

As explained above, the overlapping zone and thus also the boundary of the finer grid is placed in the medium with larger S -wave speed. Assume that the grid spacing h of the finer grid sufficiently oversamples the chosen minimum wavelength in the faster medium. Then it should be feasible to update the field values at the finer-grid boundary (blue grid positions) with the interior second-order FD scheme. This obviously requires also field values at the yellow grid positions. These values are obtained by interpolation. The bilinear interpolation (e.g. Press *et al.* 2007) is applied to the z -particle-velocity component and xz - and yz -stress-tensor components at one horizontal grid plane of the yellow grid positions (The yz -stress-tensor component is not shown in Fig. 2).

Note that the application of the second-order interior FD scheme to the finer-grid boundary significantly reduces the spatial extent of interpolation—the interpolation is applied within one grid plane. If the fourth-order scheme was applied, the interpolation would have to be applied at three grid planes.

3.2 Boundary of the coarser grid in the overlapping zone

In the overlapping zone, placed in the medium with the larger wave speed, the theoretically minimum wavelength that can propagate in the finer grid is $\lambda_N(h) = 2h$. In the same medium, the theoretically minimum wavelength that can propagate in the coarser grid is $\lambda_N(H) = 2H = (H/h)\lambda_N(h)$. Thus we have

$$0 < \lambda_N(h) < \lambda_N(H). \quad (1)$$

Therefore, the wavelengths larger than $\lambda_N(h)$ but smaller than $\lambda_N(H)$, present, in general, in the finer grid, cannot propagate from the finer grid into the coarser grid. The wavefield from the finer grid enters the coarser grid through field values at the red-circumscribed green positions. It is clear then that we cannot simply take the finer-grid field values at those red-circumscribed green positions when updating the field values at the internal grid positions (in red) of the coarser grid. The finer-grid field values at the red-circumscribed green positions have to be downsampled before they are used to update the field values at the internal grid positions of the coarser grid.

Probably the best option is to apply the Lanczos downsampling filter (e.g. Duchon 1979; Turkowski & Gabriel 1990). For brevity and simplicity of the mathematical expressions we can denote the grid ratio as

$$n = H/h. \quad (2)$$

The Lanczos filter can be expressed as

$$w_{kl}^L = A \cdot \text{sinc}\left(\pi \frac{k}{n}\right) \text{sinc}\left(\pi \frac{l}{n}\right) \text{sinc}\left(\pi \frac{\sqrt{k^2 + l^2}}{n} / 2\right); \quad (3)$$

$$|k| \leq 2n, |l| \leq 2n.$$

Here, the scaling factor A is determined by condition

$$\sum_{k=-2n}^{2n} \sum_{l=-2n}^{2n} w_{kl}^L = 1. \quad (4)$$

Then the filtered value of a field variable Φ at the grid position (i, j) of the finer grid, $\bar{\Phi}(i, j)$, is obtained as

$$\bar{\Phi}(i, j) = \sum_{k=-2n}^{2n} \sum_{l=-2n}^{2n} w_{kl}^L \Phi(i+k, j+l). \quad (5)$$

The filtration is applied in a horizontal grid plane. This is reasonable because the filtered values only enter the FD approximations to spatial derivatives in the vertical direction.

Thus, we work with two field values at each red-circumscribed green position. One is the finer-grid value $\Phi(i, j)$. The other is obtained by application of the Lanczos downsampling filter, $\bar{\Phi}(i, j)$ (5) and enters the updating of the coarser-grid field values.

Note that the application of the filter is not restricted to the velocity–stress formulation. The algorithm would be the same if grid positions of the particle-velocity components would be positions of the displacement components.

3.3 Non-reflecting boundary of the discontinuous grid

Here we only briefly comment on the contact of the overlapping zone with the non-reflecting boundary of the grid. As explained in Section 3.1, in our grid we interpolate only the z -component of the particle velocity from the three particle-velocity components. Correspondingly, the z -particle-velocity component has to be at the leftmost/rightmost/rear-most front grid positions. In other words, the outer boundary of the grid goes through the grid positions of the normal stress-tensor components. The bilinear interpolation (e.g. Press *et al.* 2007) requires values at certain grid positions around the interpolated position. If some of those positions are not available, which is the case near the outer boundary of the grid, it is necessary to apply an extrapolation instead of interpolation.

It follows from formula (5) that the downsampling can be applied at a grid position if the field values at n neighbouring grid positions from each side are available. Such neighbourhood is not available for the coarser-grid positions near the grid boundary. Therefore, the finer-grid field values at those positions have to be taken when updating the field values at the internal grid positions (in red) of the coarser grid. We have not observed effects of those direct finer-grid field values taken from the relatively very small number of such grid positions. If the non-reflecting boundary is placed inside a Perfectly Matched Layer (PML), a potential effect (if any) is likely sufficiently eliminated. We always apply the PML (Kristek *et al.* 2009).

4 NUMERICAL EXAMPLES

Here, we demonstrate our algorithm for the spatial discontinuous grid in two cases—a homogeneous half-space and a structurally complex model of the deep sedimentary valley in Grenoble, France.

The viscoelastic half-space is defined by the P -wave and S -wave speeds specified at the reference frequency of 1 Hz, 5000 m s^{−1} and 2600 m s^{−1}, density 2600 kg/m³ and frequency-independent P -wave and S -wave quality factors, 400 and 200. The rheology is represented by the generalized Maxwell Body in definition by Emerich & Korn (1987) (equivalent to the generalized Zener Body). The frequency-independent quality factors are approximated using four relaxation mechanisms in the frequency range of $<0.014, 7.0>$ Hz (Kristek & Moczo 2003; Moczo & Kristek 2005; Moczo *et al.* 2007).

The wavefield is generated by a single force acting at one point at the free surface in the vertical (z) direction, positive

downward. Its time function is given by Gabor signal, $s(t) = \exp\{-[\omega(t - t_s)/\gamma]^2\} \cos[\omega(t - t_s) + \theta]$; $\omega = 2\pi f_p$, $t \in (0, 2t_s)$, with $f_p = 1$ Hz, $\gamma = 1.5$, phase shift $\theta = 0$ and $t_s = 1.4$ s.

A discontinuous spatial grid is applied with the finer-grid spacing $h = 30$ m and coarser-grid spacing $H = 90$ m. The numbers of grid cells in the x , y and z directions are 337, 481 and 19 in the finer grid and 113, 161 and 107.5 in the coarser grid. The thickness of the overlapping zone in the z direction is $1.5 H$. The single vertical force is applied at the gridpoint [168, 168, 0] (finer-grid indices). The receiver position is at the gridpoint [305, 154, 0] (the finer-grid indices). The PML (Kristek *et al.* 2009) is applied at the boundaries of the grid to prevent spurious reflections. The second-order in time and space scheme is applied in the PML. 30 000 time levels were computed with the time step $dt = 0.002$ s.

Results of the numerical simulations for the single vertical force acting at the free surface of a homogeneous viscoelastic half-space without and with application of the Lanczos downsampling filter are illustrated in Fig. 3. The upper left part of the figure shows the total energy in the interior part of the grid (the PML is not included in the evaluation) as a function of time and time levels. The total energy is defined as

$$E = \frac{1}{2} \rho |v|^2 + \frac{1}{2} \sigma_{ij} \varepsilon_{ij}, \quad (6)$$

where ρ is density, $|v|$ magnitude of particle-velocity, σ_{ij} stress-tensor component and ε_{ij} strain-tensor component. The energy increases due to instability in the simulation without application of the Lanczos filter (the curve in red). The instability does not arise in the simulation with the Lanczos filter applied (the curve in blue). The upper right part of the figure illustrates time histories of the vertical component of the particle velocity. Here, we also included a solution obtained for the same physical problem using the uniform spatial grid with a grid spacing equal to that of the finer grid (the velocity seismogram in black). Development of the numerical noise in the simulation without the application of the Lanczos filter at the free surface is illustrated in the lower part of the figure. Three snapshots show the vertical component of the particle velocity at the free surface at times of 30, 40 and 50 s. The numerical noise appears relatively late after the useful part of the wavefield. The noise eventually unlimitedly increases and causes the instability.

The second numerical example relates to the numerical-modelling comparative exercise described in detail in the paper by Chaljub *et al.* (2010). The exercise was focused on the numerical prediction of seismic motion in the Grenoble valley, France. The Grenoble valley is a typical deep alpine sedimentary valley with complex 3-D geometry and large velocity contrasts. The article by Chaljub *et al.* (2010) presents in detail the structural model, the

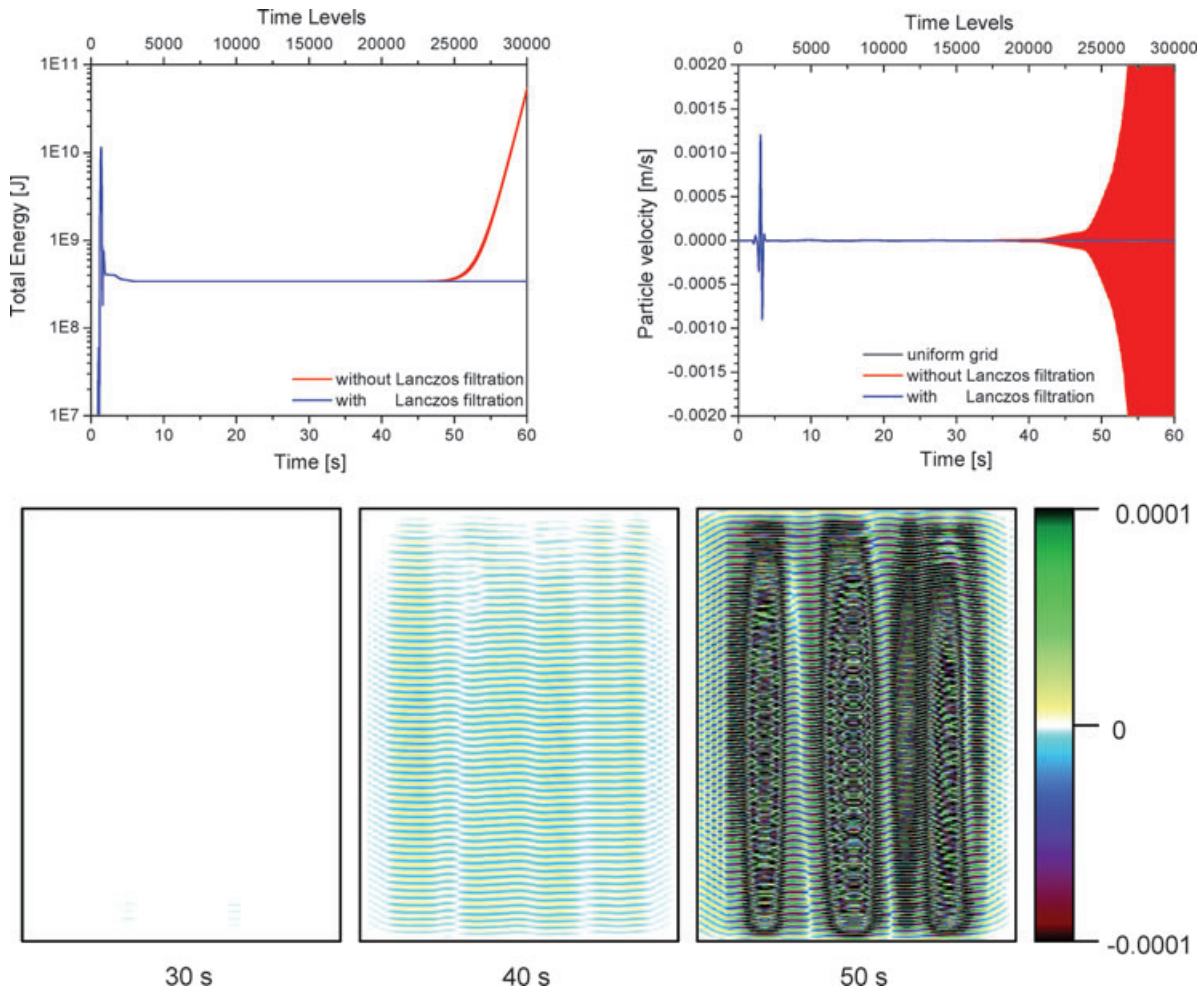


Figure 3. Results of simulations for the single vertical force at the free surface of a homogeneous viscoelastic half-space without and with application of the Lanczos filter in the algorithm of the spatial discontinuous grid with $H/h = 3$. Upper left panel: total energy in the interior part of the grid (PML not included) as a function of time and time levels. Upper right panel: time histories of the vertical component of the particle velocity. The solution obtained with a uniform fine grid is also shown for comparison. Lower part: snapshots of the vertical component of the particle velocity at three time levels.

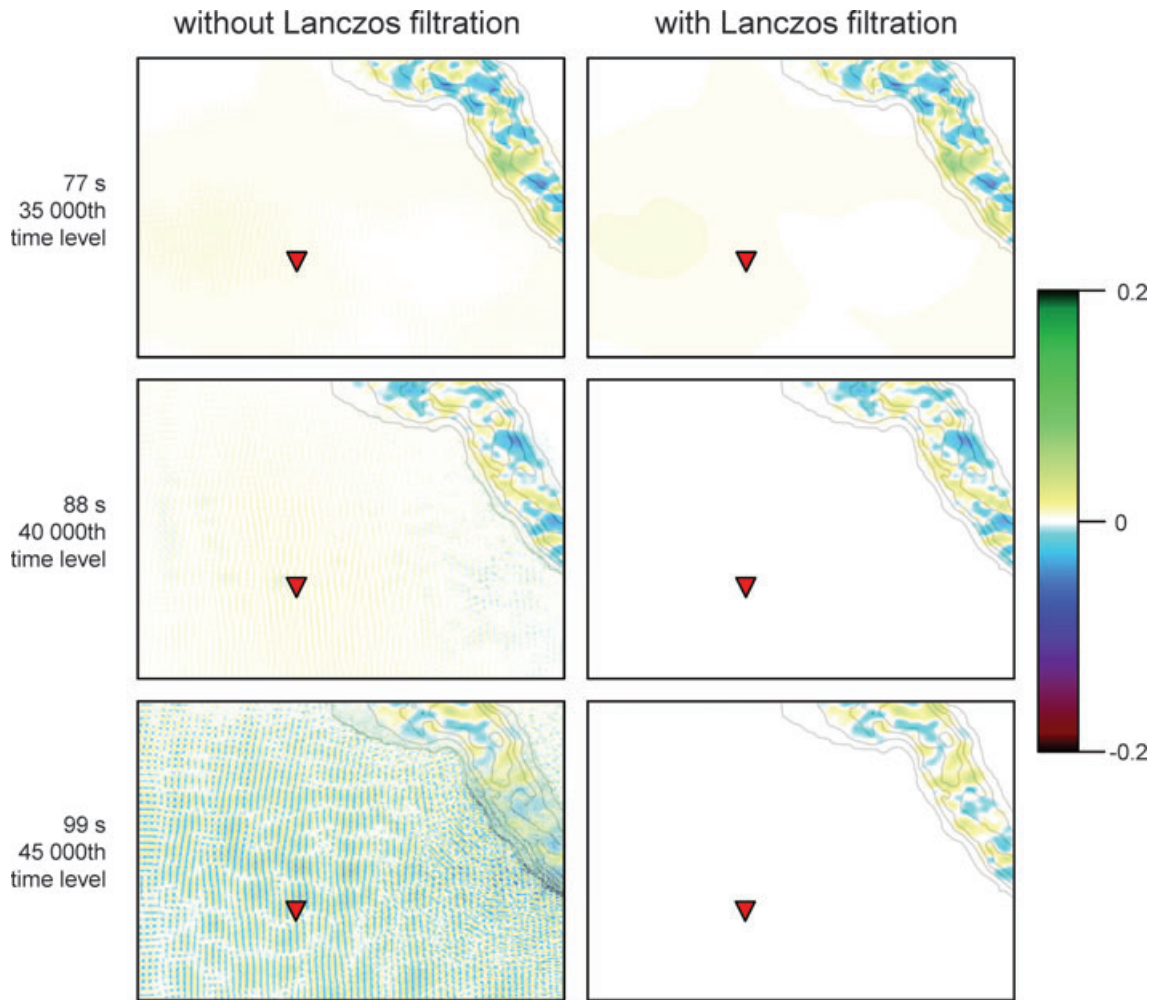


Figure 4. Snapshots of the NS component of the particle velocity at the free surface of a part of the model of the Grenoble valley, France. The contour lines indicate the sediment-bedrock interface. The snapshots in the left column illustrate development of the artificial numerical noise in the simulation without application of the Lanczos-downsampling filter. Snapshots in the right column illustrate the simulation with application of the Lanczos filter.

applied numerical methods (the spectral-element, FD and arbitrary high-order derivative—discontinuous Galerkin) and both the quantitative analysis and comparison of the four numerical predictions obtained by the three methods for the same structural model of the Grenoble valley. A surprisingly good level of agreement among the numerical solutions was found despite the very different methods and structural complexity of the model.

The FD prediction was obtained using the algorithm of the discontinuous spatial grid described in this paper. The algorithm of the discontinuous grid, however, is not described in the article by Chaljub *et al.* (2010). Neither are present snapshots shown in Fig. 4 of this paper. Fig. 4 shows snapshots of the NS component of the particle velocity at the free surface for two simulations using the spatial discontinuous grid with the grid ratio $H/h = 5$ and the contact of two grids located $1.5 H$ beneath the sedimentary valley in the bedrock. The snapshots in the left column illustrate development of the artificial numerical noise in the simulation without application of the Lanczos downsampling filter. The snapshots in the right column illustrate the simulation with the Lanczos filter applied. The difference between the two simulations is obvious. The numerical noise in the simulation without the Lanczos filter considerably affects the seismic motion in the bedrock and sediments. The two simulations are also illustrated in Fig. 5. Fig. 5 shows time histories

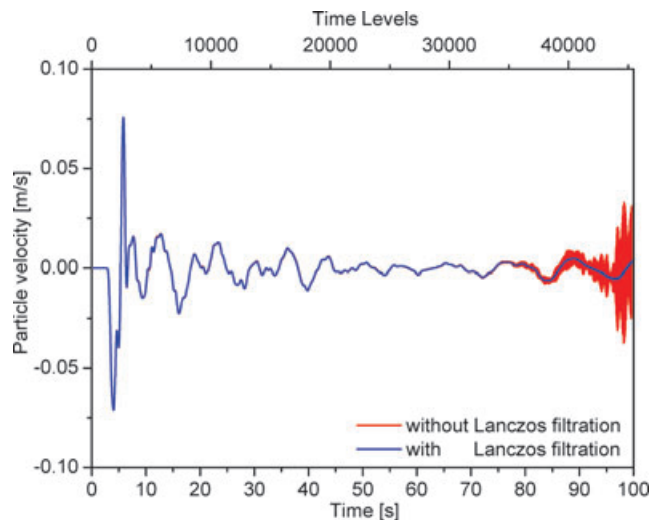


Figure 5. Time histories of the NS component of the particle velocity at the free-surface position indicated by the red triangle in Fig. 4.

of the NS component of the particle velocity at the free-surface position indicated by the red triangle in Fig. 4. As with the snapshots, the difference between the simulations without and with the application of the Lanczos filter is obvious.

5 CONCLUSIONS

We have developed an algorithm of the spatial discontinuous grid for the 3-D fourth-order velocity–stress staggered-grid FD modelling. The ratio between the grid spacing of the coarser and finer grids can be an arbitrary odd number. The key feature of the algorithm is the application of the Lanczos downsampling filter. The algorithm allows for large numbers of time levels without inaccuracy and possible eventual instability due to numerical noise that is generated at the contact of the two grids with different spatial-grid spacings.

The algorithm of the discontinuous grid is directly applicable also to the displacement-stress staggered-grid FD scheme.

We demonstrated the performance of the algorithm with the simulations of the wave propagation due to the single vertical force acting at the free surface of the homogeneous viscoelastic half-space and with the simulations of the seismic motion in the structurally complex model of the Grenoble valley, France.

The concept of the Lanczos downsampling filter is general and robust—its effect on the stability should not be dependent on a particular algorithm of the discontinuous grid.

ACKNOWLEDGMENTS

This work was supported in part by the Slovak Research and Development Agency under the contract No. APVV-0435-07 (project OPTIMODE). We also gratefully acknowledge the funding by the European Union through the Initial Training Network QUEST (grant agreement 238007), a Marie Curie Action within the ‘People’ Programme.

REFERENCES

- Aoi, S. & Fujiwara, H., 1999. 3D finite-difference method using discontinuous grids, *Bull. seism. Soc. Am.*, **89**, 918–930.
- Chaljub, E., Capdeville, Y. & Vilotte, J.-P., 2003. Solving elastodynamics in a fluid-solid heterogeneous sphere: a parallel spectral element approximation on non-conforming grids, *J. Comput. Phys.*, **187**, 457–491.
- Chaljub, E., Moczo, P., Tsuno, S., Bard, P.-Y., Kristek, J., Käser, M., Stupazzini, M. & Kristekova, M., 2010. Quantitative comparison of four numerical predictions of 3D ground motion in the Grenoble Valley, France, *Bull. seism. Soc. Am.*, **100**, 1427–1455.
- Collino, F., Fouquet, T. & Joly, P., 2006. Conservative space-time mesh refinement methods for the FDTD solution of Maxwell’s equations, *J. Comput. Phys.*, **211**, 9–35.
- De Lilla, A., 1997. Finite difference seismic wave propagation using discontinuous grid sizes, *MSc thesis*, Massachusetts Institute of Technology, Massachusetts.
- Duchon, C.E., 1979. Lanczos filtering in one and two dimensions, *J. Appl. Meteorol.*, **18**, 1016–1022.
- Emmerich, H. & Korn M., 1987. Incorporation of attenuation into time-domain computations of seismic wave fields, *Geophysics*, **52**, 1252–1264.
- Hayashi, K., Burns, D.R. & Toksöz, M.N., 2001. Discontinuous-grid finite-difference seismic modeling including surface topography, *Bull. seism. Soc. Am.*, **91**, 1750–1764.
- Jastram, C. & Behle, A., 1992. Acoustic modeling on a grid of vertically varying spacing, *Geophys. Prospect.*, **40**, 157–169.
- Jastram, C. & Tessmer, E., 1994. Elastic modelling on a grid with vertically varying spacing, *Geophys. Prospect.*, **42**, 357–370.
- Kang, T.-S. & Baag, Ch.-E., 2004a. Finite-difference seismic simulation combining discontinuous grids with locally variable timesteps, *Bull. seism. Soc. Am.*, **94**, 207–219.
- Kang, T.-S. & Baag, Ch.-E., 2004b. An efficient finite-difference method for simulating 3D seismic response of localized basin structures, *Bull. seism. Soc. Am.*, **94**, 1690–1705.
- Kopriva, D.A., 1989. Computation of hyperbolic equations on complicated domains with patched and overset chebyshev grids, *SIAM J. Sci. Stat. Comput.*, **10**, 120–132.
- Kristek, J. & Moczo, P., 2003. Seismic wave propagation in viscoelastic media with material discontinuities – a 3D 4th-order staggered-grid finite-difference modeling, *Bull. seism. Soc. Am.*, **93**, 2273–2280.
- Kristek, J., Moczo, P., Irikura, I., Iwata, T. & Sekiguchi, H., 1999. The 1995 Kobe mainshock simulated by the 3D finite differences, in *The Effects of Surface Geology on Seismic Motion*, Vol. 3, pp. 1361–1368, eds. Irikura, K., Kudo, K., Okada, H. and Sasatani, T., Balkema, Rotterdam.
- Kristek, J., Moczo, P. & Galis, M., 2009. A brief summary of some PML formulations and discretizations for the velocity-stress equation of seismic motion, *Stud. Geophys. Geod.*, **53**, 459–474.
- Moczo, P., Bystrický, E., Kristek, J., Carcione, J.M. & Bouchon, M., 1997. Hybrid modeling of P-SV seismic motion at inhomogeneous viscoelastic topographic structures, *Bull. seism. Soc. Am.*, **87**, 1305–1323.
- Moczo, P. & Kristek, J., 2005. On the rheological models used for time-domain methods of seismic wave propagation, *Geophys. Res. Lett.*, **32**, L01306, 1–5.
- Moczo, P., Labák, P., Kristek, J. & Hron, F., 1996. Amplification and differential motion due to an antiplane 2D resonance in the sediment valleys embedded in a layer over the halfspace, *Bull. seism. Soc. Am.*, **86**, 1434–1446.
- Moczo, P., Kristek, J., Galis, M., Pazak, P. & Balazovjech, M., 2007. The finite-difference and finite-element modeling of seismic wave propagation and earthquake motion, *Acta Phys. Slovaca*, **57**, 177–406.
- Press, W.H., Teukolsky, S.A., Vetterling, W.T. & Flannery, B.P., 2007. *Numerical Recipes*, Cambridge University Press, Cambridge.
- Robertsson, J.O.A. & Holliger, K., 1997. Modeling of seismic wave propagation near the Earth’s surface, *Phys. Earth planet. Inter.*, **104**, 193–211.
- Turkowsky, K. & Gabriel, S., 1990. Filters for common resampling tasks, in *Graphics Gems I*, ed. Glassner, A.S., pp. 147–165, Academic Press, San Diego.
- Wang, Y. & Schuster, G.T., 1996. Finite-difference variable-grid scheme for acoustic and elastic wave equation modeling, in *Proceedings of the 66th Ann. Intl. Mtg., Soc. Expl. Geophys., Expanded Abstracts*, Denver, Colorado, 10–15 November 1996, pp. 674–677.
- Wang, Y. & Takenaka, H., 2001. A multidomain approach of the Fourier pseudospectral method using discontinuous grid for elastic wave modeling, *Earth Planets Space*, **53**, 149–158.
- Wang, Y., Xu, J. & Schuster, G.T., 2001. Viscoelastic wave simulation in basins by a variable-grid finite-difference method, *Bull. seism. Soc. Am.*, **91**, 1741–1749.